2024 EAGE ANNUAL 85TH CONFERENCE & EXHIBITION OSLO | NORWAY

FWI imaging through basalts

N. Shah[2], M. Warner[1], T. Nangoo[2], A. Umpleby[2], J. Reilly[2], J. Buehnemann[3], T. Roth[3], J. Fowler[4], N. Huebner[4]

[1] Imperial College London; [2] S-Cube London; [3] Wintershall Dea AG; [4] Wintershall Dea Norge AS

Summary

We apply adaptive waveform inversion, reflection waveform inversion and broadband FWI imaging to conventional narrow-azimuth towed-streamer seismic data acquired over a deep-water heterogeneous basaltic section. The resulting high-resolution velocity model reveals the structure and physical properties of the basaltic layers in the sub-surface. Spatial differentiation of the broadband acoustic-impedance model recovered using short-offset 60-Hz FWI applied to the unprocessed field data generates a multiple-free deghosted true-amplitude depth-migrated image of acoustic reflectivity. The image is significantly superior to the existing conventional PSDM generated using conventional processing. Parameter selection and real-time dynamic control of the inversion are automated, driven using measurements on data and model that include local phase differences between predicted and observed data weighted by amplitude envelope.

FWI imaging through basalts

Introduction

Full-waveform inversion now forms a routine part of the great majority of depth-imaging processing sequences for all types of marine seismic data, and it is being applied to good effect for even the most challenging deep-target, sub-salt, node datasets. Several simultaneous technical developments have made these advances possible (Warner et al., 2023). These include: (1) FWI objective functions that are unaffected by cycle skipping, (2) robust forms of reflection FWI that are able to extract accurate long-wavelength velocity updates from small variations in reflection moveout, (3) broad-bandwidth FWI reflectivity imaging from raw field data that can replace conventional PSDM, (4) automated FWI parameter tuning and workflows that require minimal intervention, and (5) data preconditioning combined with robust objective functions that together are able to extract maximum utility and accuracy from purely acoustic FWI when applied to elastic field data. Warner et al. (2022) have previously shown that acoustic FWI can also extract accurate elastic AVA parameters directly from field data.

Here, we demonstrate these advances when FWI is applied to limited-offset, narrow-azimuth, towed-streamer data acquired to image beneath complex basaltic flows and intrusions. Unlike sub-salt imaging, where the principal challenge is to determine salt geometry, in sub-basalt imaging both the basalt geometry and its heterogeneous internal properties can prove equally challenging. In addition, intrinsic and scattering transmission losses can be significant within inter-layered weathered and altered basaltic sequences. Consequently, FWI has great potential to improve sub-basalt imaging, but the complexities of basaltic overburden typically require a combination of the full range of advanced FWI technologies in order to exploit that potential. The limited offset of NATS data especially requires a robust combination of objective functions able to exploit the kinematics of limited-offset reflections.

Dataset and workflow

Baldock et al. (2022) have previously demonstrated that FWI can improve velocity models within basaltic sections; here we show that FWI can both build the velocity model from scratch, and can generate a final reflectivity volume. We used data from a relatively conventional 3D NATS survey in the Norwegian Sea, employing 8-km slanted cables, in about 1.5 km of water. Basalts, of poorly known thickness and geometry, lie within a few hundred metres of the seabed. There are no wells. Exploration interest is within about 3 km of the seabed. Figure 1 shows a typical raw shot record after low-pass filtering at 20 Hz. These data are dominated by reflections and their strong surface multiples. There are weak, fast, early refracted arrivals visible in the data that are likely generated within shallow basalts; surface multiples of some of these refractions are also apparent. The refracted arrivals are relatively high frequency, do not penetrate far into the subsurface, and do not normally extend to the maximum 8-km length of the streamer. Most of the strongest events in the section are near-critical or post-critical reflections together with their surface multiples; these wide-angle events will almost certainly be significantly affected by the shear properties of the subsurface and so prove challenging for acoustic FWI. Figure 2 shows an existing velocity model together with its associated conventional PSDM image. While we do not know the exact genesis of this model, it is not FWI-based, and the shallow high-velocity basaltic sequence it contains has likely been inserted manually. The PSDM shows significant systematic loss of high frequencies with increasing depth. Deeper primary reflectivity is unclear, and the section shows short-wavelength structure in many reflectors that is likely produced by shallower basalt-related velocity heterogeneity that has not been captured within the rather smooth legacy model.

FWI proceeded via three inter-linked stages, iterating successively from 4 to 40 Hz. In the first stage, adaptive waveform inversion, AWI, was used to build the near-seabed and shallowest-basalt velocity structure. AWI has immunity to cycle skipping, enhanced sensitivity to reflection moveout, and reduced sensitivity to amplitude mismatches – especially those produced by unmodelled attenuation and elastic phenomena. In the second stage, AWI is combined with reflection waveform inversion, RWI. This alternates repeatedly between short-wavelength reflectivity imaging inverting for acoustic impedance, and longer-wavelength velocity modelling in which density passively tracks the velocity model. Both

steps here seek principally to match the kinematics of the wavefield; the reflectivity model is regenerated explicitly at every outer RWI iteration. RWI takes place with surface-multiples, interbed multiples and surface ghosts all retained within the input data. These are modelled during FWI, and the multiples as well as the primary reflections contribute to the imaging and to the macro-velocity updates. In stage three, true-amplitude, alternating AWI and FWI imaging of acoustic reflectivity is undertaken in the target zone. This was run to a maximum frequency of 60 Hz. Only short-offset reflections are included at this final stage since their amplitudes are only minimally affected by elastic AVA such that a lower-cost acoustic wave equation can reliably reproduce their dynamics.

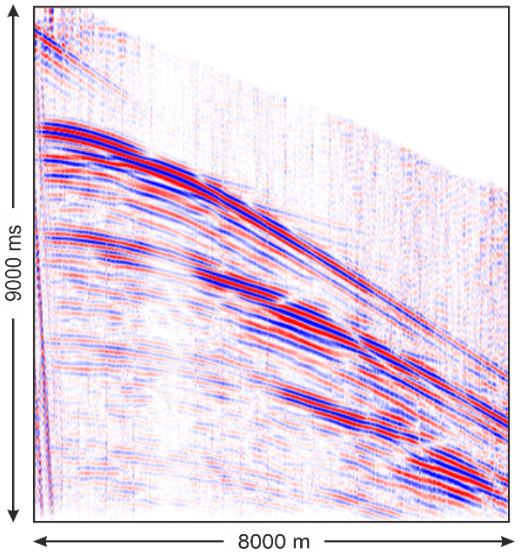

Figure 1 *Raw shot record after 20-Hz low-pass filter.*

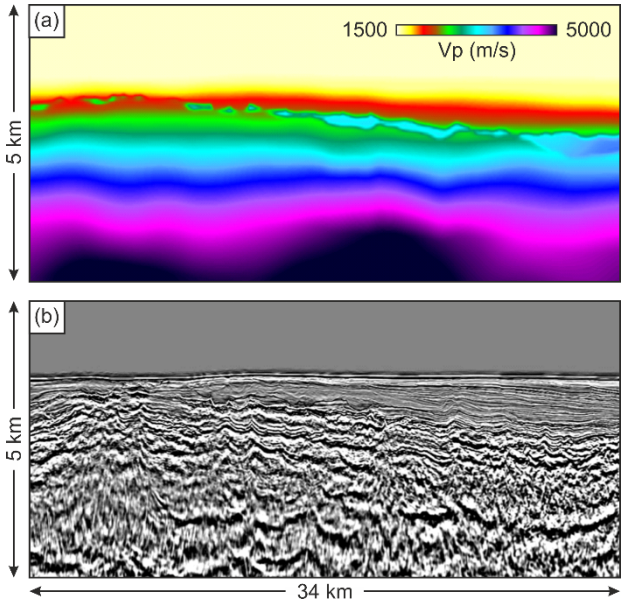

Figure 2 *(a) Legacy velocity model. (b) Corresponding legacy PSDM.*

Results

Figure 3 shows results from the integrated AWI-RWI-FWI workflow displayed at successive frequencies. The size, location, and colour scale used here are the same as those used in Figure 2a. The simple smooth starting model used did not contain any representation of the geometry of the basaltic layers. The colour images merge both the long-wavelength velocity models and the short-wavelength acoustic impedance models, with the latter rescaled into velocity using a modified form of Gardner's law. The grey-scale reflectivity images show the spatial differential of the full acoustic-impedance model. These images show the true acoustic reflectivity which does not depend upon any assumptions about the local relationship between velocity and density, and is not significantly influenced by elastic effects. The magnitude of the reflectivity is however affected by assumptions about anelastic and small-scale scattering attenuation, and is band-limited by the maximum frequency used during FWI.

The velocity model evolves significantly to about 20 Hz. Thereafter, the appearance of the macro-velocity model does not change significantly since it has already captured almost all of the long wave-length dynamics of the data. Continued iteration to higher frequencies continues to sharpen the model, and this continues to improve the FWI-derived reflectivity model. For the deeper portion of the model, there is little primary energy above about 40 Hz so that continued iteration to 60 Hz continues to sharpen only the upper portions of the model. In the deeper section, iteration beyond 40 Hz predominantly serves to introduce high-frequency noise; this is a fundamental limitation of the bandwidth of this field data that is presumably related to transmission losses through the shallow section.

It is clear that sub-basalt reflectivity in the FWI image is much less affected by unmodelled shallow velocity anomalies than is the conventional legacy PSDM image shown in Figure 2a. The reflectivity revealed by FWI is more continuous, and is almost everywhere much less undulating than the PSDM.

The deep reflectivity in the FWI image is significantly enhanced. The FWI image appears to be unaffected by surface-multiple contamination despite the fact that it is generated using raw field data that contain a full suite of multiples. In contrast, for the PSDM it is difficult to be sure that there is no multiple contamination at depth despite the fact that the image was generated from pre-processed data.

Figure 4b illustrates one form of quality control that was used to automate critical parameter choices during FWI, to control the range of offsets and temporal bandwidth used at each iteration, and to automate switching between different formulations of AWI, RWI and FWI. It can also serve as a simple human QC during inversion runs to provide an early indication of potential problems. Figure 4a shows a conventional shot record in which field and predicted data have been interleaved. Figure 4b shows the local phase difference between field and predicted data for the same shot record – yellow indicates a good match, blue that the predicted data are early, and red that they are late. Colour intensity is modulated by the local amplitude envelope. This phase-difference volume is fast to generate, simple to interrogate automatically, and independent of the objective function used to drive the inversion. It can thus serve as an independent means to automate almost all aspects of the inversion.

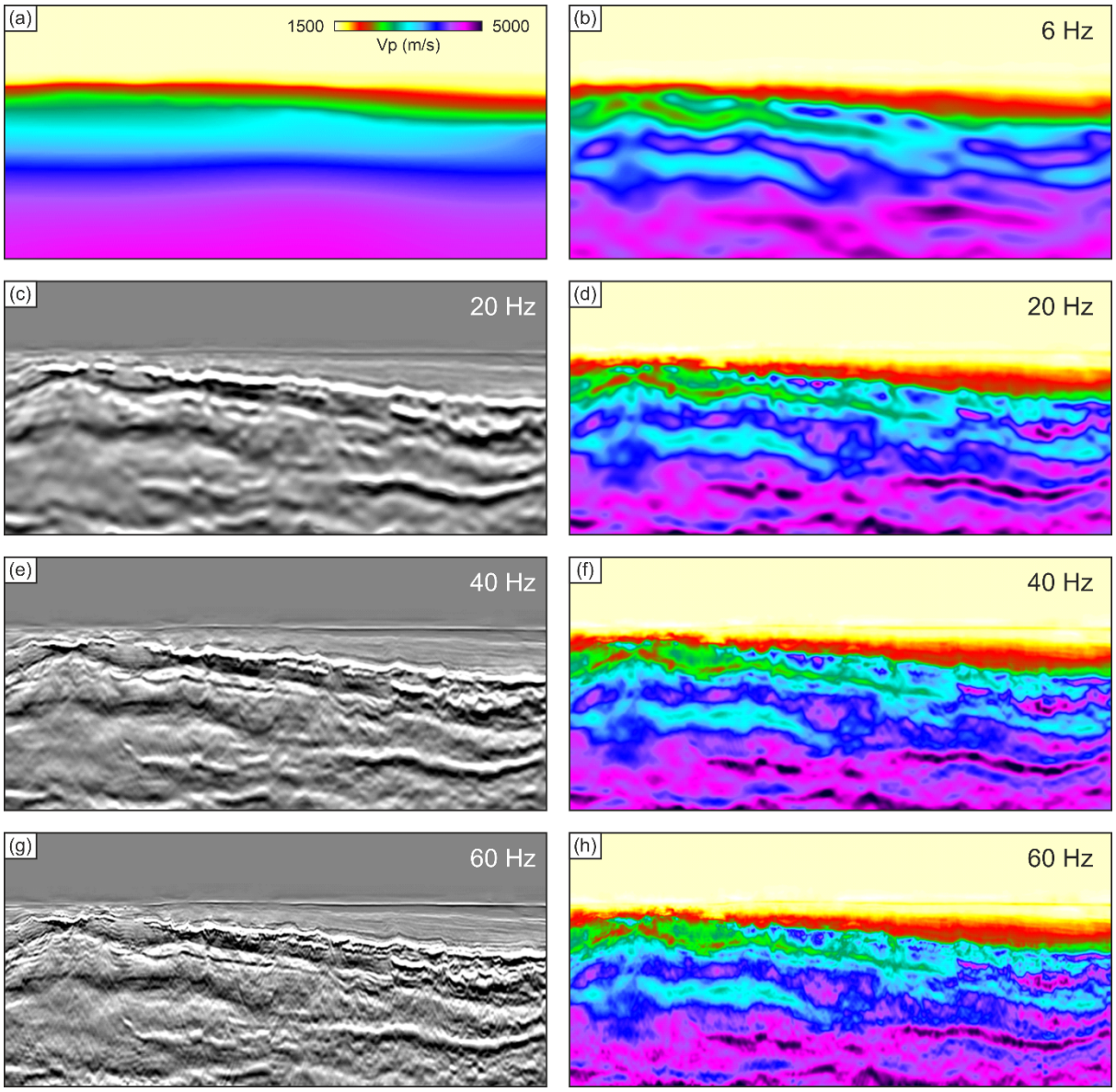

Figure 3 *Results of FWI. Colour images show velocity; grey-scale images show acoustic reflectivity derived from the FWI model. (a) Starting velocity model. (b) Low-frequency velocity model recovered by AWI-RWI. (c-h) Successive reflectivity and velocity models as the inversion frequency is increased.*

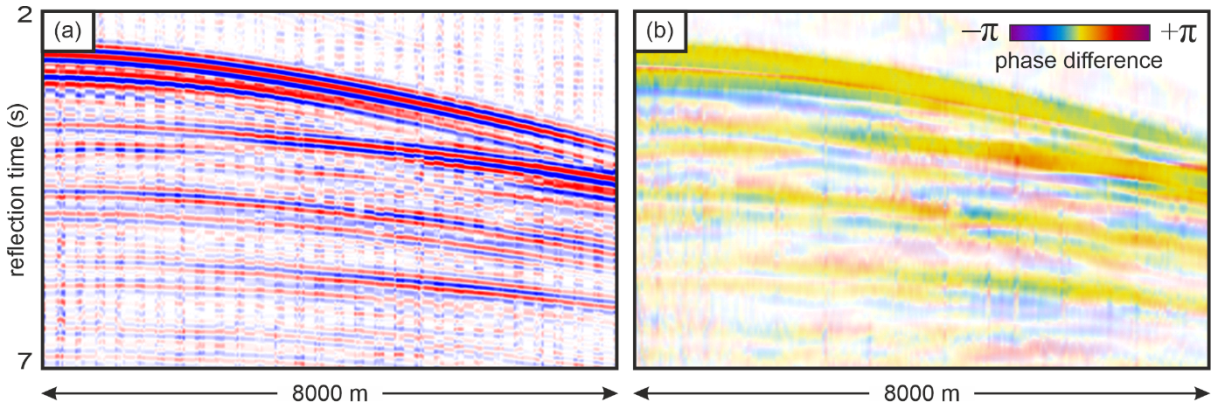

Figure 4 *(a) Interleaved field and predicted data, for one shot record, part way through AWI-RWI. (b) Local phase difference between field and predicted data for the same shot record. Colour intensity scales with local amplitude; hue varies with phase, yellow indicates no phase difference. Similar information is available in both displays, but decisions are simple to automate using (b).*

Conclusions

We have shown that it is possible to image usefully beneath basalts using appropriate forms of FWI applied to reflection-dominated narrow-azimuth towed-streamer data. To achieve this, beginning from a simple featureless starting model, it is necessary to employ a version of FWI that is robust against cycle skipping, and that can use small variations in reflection moveout to update the macro-velocity model. If this is to be achieved at reasonable cost using acoustic FWI, then appropriate mitigation of elastic effects is required throughout, especially if the field data contain long-period post-critical multiples. Here, a three-stage approach was used to achieve this. Shallow AWI was applied to match turning-ray kinematics, followed by combined AWI and RWI applied to reflection and multiple kinematics, and the inversion completed using limited-offset true-amplitude FWI run to high frequency.

AWI overcomes cycle skipping, and resolves heterogenous overburden with strong velocity contrasts. Combined AWI-RWI separates the inversion kernel into an acoustic-impedance reflectivity image and a macro-velocity update, and matches the details of reflection and multiple moveout. Broad-bandwidth FWI sharpens the final image and matches short-offset reflection amplitudes. Spatial differentiation of the resulting acoustic-impedance model then directly generates a multiple-free, deghosted, true amplitude, acoustic-reflectivity, depth image. That image was significantly superior to an existing conventional PSDM image. We used local phase differences to automate parameter selection and to control FWI dynamically as the inversion proceeded. The final result was produced without bias from a starting model, and without insertion of picked basalt layers; decisions were driven directly by the data. The approach works on legacy streamer data without long-offsets, low frequencies, or wide azimuths.

Acknowledgements

The authors would like to thank the data owners Wintershall Dea Norge AS, and the license partners Aker BP ASA and INPEX Idemitsu Norway AS, for their kind permission to publish this work.

References

Baldock et al. [2022] Sub-basalt imaging in the NW Europe Atlantic margin. *84th EAGE Conference and Exhibition*, Extended Abstracts.

Warner et al. [2022] AVO determination using acoustic FWI. *84th EAGE Conference and Exhibition*, Extended Abstracts.

Warner et al. [2023] Automated salt model building. *The Leading Edge*, **42**(3), 196-206.